ACCSCIENCE PUBLISHING

International Journal of Bioprinting

RESEARCH ARTICLE

3D-bioprinted osteochondral model based on hierarchical polymeric microarchitectures for *in vitro* osteoarthritis drug screening

Yi-Cheng Wang[1†], Xiao-Jie Song[1†], Xiao-Chang Lu[1], Zhou-Jiang Chen[2], Yue-Wei Li[1], Ranjith Kumar Kankala[1], Ai-Zheng Chen[1], Shi-Bin Wang[1*], and Chao-Ping Fu[1*]

[1]Institute of Biomaterials and Tissue Engineering & Fujian Provincial Key Laboratory of Biochemical Technology, Huaqiao University, Xiamen, Fujian, China

[2]Engineering Research Center for Pharmaceuticals and Equipment of Sichuan Province, Sichuan Industrial Institute of Antibiotics, School of Pharmacy, Chengdu University, Chengdu, Sichuan, China

(This article belongs to the *Special Issue*: *Advanced Strategies in 3D Bioprinting for Disease Modelling*)

Abstract

Compared to conventional two-dimensional (2D) or scaffold-free three-dimensional (3D) drug screening models, biomimetic osteochondral constructs offer superior physiological relevance for studying osteoarthritis (OA) and accelerating therapeutic discovery. This study reports the development of a polymeric microarchitecture (PM)-based 3D osteochondral model for drug screening applications. Microfluidics-assisted fabrication enabled the generation of cartilage-like and osteogenic microtissues by encapsulating chondrocytes and endothelial/osteoblast cells within PMs. These multicellular aggregates were embedded in gelatin methacryloyl and assembled via 3D bioprinting into a stratified osteochondral construct. The model exhibited favorable cell viability, high proliferation, and organized microtissue formation, validating its biological functionality. An OA-like microenvironment was induced using lipopolysaccharide, significantly elevating pro-inflammatory cytokines. Treatment with diclofenac, dexamethasone, or curcumin markedly attenuated this response, reducing tumor necrosis factor-alpha, interleukin (IL)-1β, and IL-6 to 42.1, 193.5, and 193.5 pg/mL, respectively, while elevating the anti-inflammatory cytokine IL-10 to 90.2 pg/mL. Overall, this PM-based 3D osteochondral platform reproduces key features of native joint tissue and holds promise for OA research, drug screening, and regenerative medicine.

***Keywords*:** 3D osteochondral model; Curcumin; Drug screening; Microfluidics; Porous microspheres

†These authors contributed equally to this work.

***Corresponding authors:**
Shi-Bin Wang (sbwang@hqu.edu.cn)

Chao-Ping Fu (fuchp@hqu.edu.cn)

Citation: Wang YC, Song XJ, Lu XC, *et al.* 3D-bioprinted osteochondral model based on hierarchical polymeric microarchitectures for *in vitro* osteoarthritis drug screening. *Int J Bioprint*. 2025;11(6):220-237. doi: 10.36922/IJB025290288

Received: July 14, 2025
Revised: August 31, 2025
Accepted: September 10, 2025
Published online: September 10, 2025

1. Introduction

Body articulation or joint-related diseases often lead to difficulties in mobility and even paralysis in some instances, seriously affecting the quality of life in patients. Among various joint-related diseases, osteoarthritis (OA) is one of the most common

degenerative diseases of the skeletal system, affecting around 85 million people globally every year.[1,2]

Articular cartilage plays a crucial role in the lubrication and protection of the joint. The development of OA is manifested by the gradual loss of the articular cartilage and the densification of the underlying subchondral bone, leading to osteophyte formation and subchondral sclerosis, or even chondrocyte apoptosis and synovial effusion.[3–6] Several treatment strategies, including the most common joint replacement surgical procedure, are sophisticated and complicated and often suggested at the advanced pathophysiological stage. In addition, chemotherapeutic assistance is provided by prescribing steroids and non-steroidal anti-inflammatory drugs (NSAIDs) for OA patients. However, the prescribed medication provides merely symptomatic pain relief, which is short-lived and transient, thereby requiring long-term therapeutic strategies for OA.[7,8] Moreover, it should be noted that most of the currently available drug candidates are still having limited efficiency. Therefore, extensive research has been conducted to develop highly efficient, cost-effective, and non-invasive strategies for OA therapy.[9,10]

The establishment of screening models is essential for the rapid development of chemotherapeutic drugs. In this vein, highly efficient preclinical models are required to achieve high-throughput drug screening and enable precise and accurate investigation of OA pathology.[11–13] Several *in vivo* models replicate OA with clinically relevant features. However, these models suffer from several limitations, such as high cost, long development periods, and handling challenges.

Numerous *in vitro* models have been developed to address these shortcomings for the efficient initial screening of therapeutic agents towards OA therapy.[14,15] Typically, the two-dimensional (2D) cell culture of chondrocytes is considered a "model cell" for investigating OA *in vitro*. Comparatively, the three-dimensional (3D) models based on chondrocytes are more reliable than the conventional 2D monolayers to investigate OA due to their simulations of cell–cell and cell–extracellular matrix (ECM) interactions. Further advancements include developing the scaffold-based 3D models as the screening platforms, enabling controlled matrix elasticity for the co-culturing of multiple cell types (including bone cells) and investigations of cell fate. Moreover, the encapsulated chondrocytes in 3D scaffolds could better maintain their physiological phenotype and thus enhance the regeneration capacity of articular cartilage compared to the 2D culture models.[16,17]

Among the joint tissues, the subchondral bone cells play a significant role in maintaining the proper cartilage matrix and the articular physiology by interacting with each other.[18,19] In a previous study, Maihemuti *et al.*[20] proposed a 3D-printed porous multilayer scaffold based on cold-water fish skin gelatin for osteoarticular cartilage regeneration of damaged cartilage after arthritis. It was demonstrated that the simulation of the physiological microstructure of articular cartilage and subchondral bone was essential to construct a 3D scaffold-based OA model. In another study, Korpayev *et al.*[21] designed a multilayer scaffold embedding chondrocytes and preosteoblastic cells as a biomimetic osteochondral model. The close simulation and construction of bone joint structure and composition would benefit the investigation of OA pathology and drug screening.[22–24]

Polymeric microarchitecture (PM)-based scaffolds have attracted enormous attention from researchers owing to their outstanding biocompatibility, excellent cell carrying capacity, and ability to facilitate ECM-like environments for cell growth.[25–27] These PMs with exceptional porosity and interconnecting windows substantially encapsulate cells and enable their infiltration into the interiors. This ensures cell survival and proliferation by enabling the passage of required nutrients for cells to survive at the PMs core. Among various polymers from natural and synthetic sources, poly(lactic-co-glycolic) acid (PLGA), a synthetic polymer approved by the United States (US) Food and Drug Administration, has garnered enormous interest in the field of biomaterials due to the favorable mechanical properties, low toxicity, and low immunogenicity.[28,29] It has been demonstrated that cells are attached more rapidly to PLGA-based PMs with a significantly enhanced growth rate compared to commercially available porcine gelatin microcarriers.[27,30–32]

Notably, these PMs can be applied for drug delivery towards joint diseases. In a study, Dhanabalan *et al.*[33] designed a rapamycin-encapsulated PLGA-based PM, demonstrating high residence time and co-localization with various joint tissues when administered in the mouse knee via intra-articular injections. Such biomaterial-based delivery of rapamycin offers great potential for testing in animal models and clinical translation as a patient-compliant treatment. The controllable spatial distribution of microsphere-based scaffolds could mimic the native tissues and thus form bone-like and cartilage-like macro-sized architectures.[34–36]

Gelatin methacryloyl (GelMA) hydrogel has emerged as an ideal biomaterial for 3D bioprinting owing to its photo-crosslinkability, excellent biocompatibility, and tunable mechanical properties. Studies have demonstrated that the density of the molecular network (DMN) of GelMA can be precisely modulated by optimizing the

degree of substitution and solid content, enabling its compressive modulus to span a wide pressure range of 3–123 kPa.[37] This versatility allows GelMA to match the mechanical characteristics of various soft tissues, such as the liver, brain, and kidney. Furthermore, by incorporating reinforcing materials, GelMA-based composites can approach the mechanical requirements of stiffer tissues, including cartilage and bone. The innate arginyl–glycyl–aspartic acid sequences in GelMA support cell adhesion and migration. Low-DMN formulations facilitate cell spreading and proliferation, supporting high cell viability (>95%), while high-DMN versions offer enhanced shape fidelity and mechanical stability, making them suitable for printing complex architectures. These attributes collectively enable GelMA to mimic the native cellular microenvironment *in vitro*, thereby reducing the need for repetitive preliminary experiments and providing a standardized platform for applications such as tissue engineering and organ-on-a-chip systems.

Lipopolysaccharide (LPS) is the most abundant component within the cell membrane of Gram-negative bacteria. It can stimulate the release of inflammatory cytokines in various cell types, leading to an acute inflammatory response toward pathogens. OA is a low-grade inflammatory condition, and the elevation of the LPS levels in obesity and metabolic syndrome could contribute to OA.[38,39]

Motivated by these considerations, we demonstrated the fabrication of an *in vitro* OA model composed of hierarchical osteochondral tissue architectures using a combinatorial approach of microfluidic technique and 3D bioprinting.[40] Initially, PMs were prepared using the microfluidic technique. Mouse embryonic chondrocytes (C518) were then embedded into the PMs to construct cartilaginous cellular microtissues (C-MTs). In addition, mouse embryonic osteoblasts (MC3T3-E1) and mouse aorta endothelial cells (MAEC) were simultaneously encapsulated in a separate batch of PMs to construct endothelial osteoblastic microtissues (EO-MTs). Then, the C-MTs and EO-MTs were mixed with GelMA as a bioink for building a hierarchical osteochondral architecture using the 3D bioprinting approach (Figure 1). OA condition was finally induced in the designed hierarchical architectures by exposing the osteochondral model to LPS.

Curcumin (Cur) is a natural anti-inflammatory agent used in treating medical conditions for many years. Several reports indicated its potency to target multiple inflammatory diseases, including OA, rheumatoid arthritis, and other inflammatory arthritic conditions.[41–43] Similarly, the synthetic glucocorticoid dexamethasone (Dex) has been widely employed in intra-articular therapy for OA due to its potent anti-inflammatory effects, effectively inhibiting pro-inflammatory cytokines, such as interleukin (IL)-6, tumor necrosis factor-alpha (TNF-α), and matrix

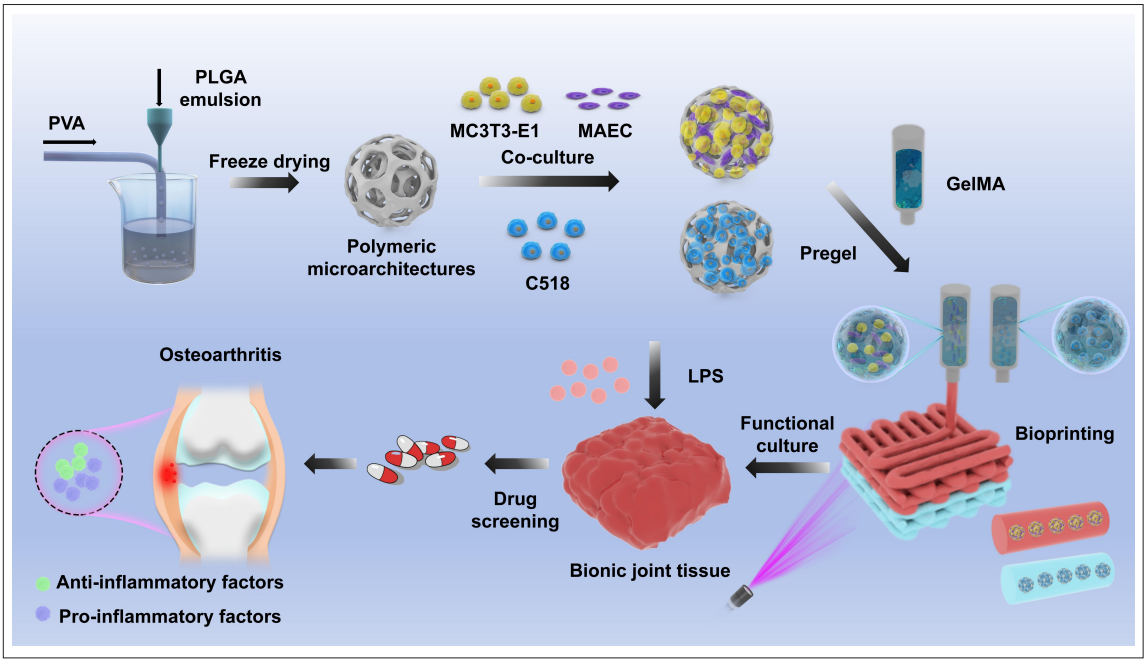

Figure 1. Schematic illustrating the preparation of hierarchical osteochondral architectures based on PLGA-based polymeric microarchitectures, fabricated through a combination of microfluidics and bioprinting technologies for drug screening. Abbreviations: GelMA, gelatin methacryloyl; LPS, lipopolysaccharide; MAEC, mouse aorta endothelial cell; PLGA, poly(lactic-co-glycolic) acid; PVA, polyvinyl alcohol.

metalloproteinases, through nuclear factor kappa-light-chain-enhancer of activated B cells pathway suppression.[44] Additionally, diclofenac (Dic), an NSAID, is commonly administered topically or orally to alleviate OA pain and inflammation by inhibiting cyclooxygenase activity.[45] Therefore, in this study, Cur, Dex, and Dic were employed as drug models for proof-of-concept to investigate the drug screening efficacy of the constructed osteochondral unit.

2. Materials and methods

2.1. Materials

Polyvinyl alcohol (PVA), PLGA (lactide:glycolide = 75:25, 66–107 kDa), gelatin, Dic, Dex, ascorbic acid, and β-glycerophosphate sodium were obtained from Sigma-Aldrich (US). Cur (99.7%) and dichloromethane were purchased from Sinopharm Group Chemical Reagent Co., Ltd. (China). Cell Counting Kit-8 (CCK-8) and 4',6-diamidino-2-phenylindole (DAPI) were purchased from Nanjing Keygen Biotech Co., Ltd. (China). The Bradford assay kit was purchased from Bio-Rad (US). Qtracker®525 and 655 Cell Labeling Kits were obtained from Thermo Fisher Scientific (US). Penicillin–streptomycin, fetal bovine serum (FBS), and Dulbecco's modified Eagle medium (DMEM) were purchased from Gibco (US).

2.2. Preparation and characterization of polymeric microarchitectures

Initially, PLGA-based PMs were prepared using a microfluidic technique, as previously reported.[30] Briefly, a customized coaxial microfluidic system was prepared using plastic tubes (inner diameter: 1 mm), a glass capillary (outer diameter: 1 mm), and a needle (27G, inner diameter: 210 μm, outer diameter: 400 μm). PLGA (180 mg) was dissolved in dichloromethane (4.5 mL), and the aqueous gelatin (6% w/v) was then added to form a water-in-oil emulsion. The initial emulsion was stabilized by ultrasonication and then introduced into the microfluidic device as the discontinuous phase, while PVA solution (1% w/v) was used as the continuous dispersion phase. The flow rates of the discontinuous and the dispersion phases were set at 0.05 and 2 mL/min, respectively. The PLGA-based PMs were subsequently collected in a pre-cooled PVA solution (1% w/v). After stabilization, the PMs were washed with deionized water at 40°C to eliminate gelatin and achieve a porous structure. Finally, the PMs were lyophilized and stored until further use.

The morphology of PMs was observed using field emission-scanning electron microscopy (FE-SEM; S-4800, HITACHI, Japan) after sputter-coating with gold. Fourier transform infrared (FTIR) spectra were obtained using a Nicolet iS50 model FTIR spectrophotometer (Thermo Nicolet Corporation, US) at a 4 cm^{-1} resolution using KBr pellets. The degradation of PMs was investigated by exposing the PMs to phosphate-buffered saline (PBS; pH 7.4) at 37°C, and the changes in the morphology of PMs at different predetermined time intervals were observed using FESEM. Furthermore, the protein adsorption efficacy of PMs was investigated using a standard Bradford assay kit. Briefly, PMs were placed in 96-well plates, and then 200 μL of 10% FBS-containing DMEM was added to each well, and the medium was replaced at predetermined time intervals. After washing with PBS, the PMs were immersed in 200 μL of protein eluent for 30 min, and the protein content was determined using the Bradford assay kit.

2.3. Preparation and characterization of cartilaginous cellular microtissues and endothelial osteoblastic microtissues

Cell lines MC3T3-E1, C518, and MAECs (Beina Biotechnology Research Institute, China) were cultured in complete medium (basal medium supplemented with 10% [v/v] FBS, 1% [v/v] penicillin–streptomycin) at 37°C in 5% CO_2 and 95% relative humidity. Firstly, PM suspension with different concentrations (0.25, 0.5, and 1 mg/mL) was prepared in DMEM and added to the cells for different incubation times. Cell viability was detected through the CCK-8 assay. C-MTs and EO-MTs were developed by encapsulating the cells in PMs separately.[32,46] For the construction of C-MTs, microspheres were placed in each well of a 96-well plate after sterilization. Then, 200 μL of C518 cell suspension at a concentration of 1.6×10^4 cells/mL was added for culturing modes. The PMs were placed in an incubator for static culture, or placed at 37°C and 110 rpm for dynamic culture under the condition of ensuring nutrition and oxygen supply. Similarly, EO-MTs were constructed by co-culturing MAECs and MC3T3-E1 cells together with PMs. After 3, 9, and 24 h of culture, non-adherent cells were removed by washing three times with PBS after removing the medium, and PMs were collected and digested with trypsin and counted. Adhesion and proliferation assays were performed using triplicate cultures, and the data were representative. The cell adhesion rate was calculated using **Equation I**, as previously reported[30]:

$$\text{Cell adhesion rate (\%)} = \text{Cell adhesion/Cell inoculation number} \times 100 \quad \text{(I)}$$

The MAECs and MC3T3-E1 cells were labeled with Qtracker®655 and Qtracker®525, respectively, and the distribution of cells in EO-MTs was observed through Leica TCS SP8 confocal laser scanning microscopy (CLSM) (Leica Microsystems GmbH, Germany). Immunofluorescence staining was used to observe

the expression of aggrecan, collagen I, and collagen II in C-MTs. The CCK-8 method was used to detect the proliferation of cells in the MTs under static and dynamic culture. The MTs were fixed with paraformaldehyde and stained with DAPI for CLSM imaging. Other MTs were embedded in paraffin and sectioned for hematoxylin and eosin (HE) staining. After dehydration with gradient ethanol solutions, the fixed sealing plates were observed using a light microscope (Nikon Eclipse Ts2, Japan). Assays were performed with triplicate cultures, and data are representative of three experiments.

Next, MAECs and MC3T3-E1 cells were co-cultured using the method described in Section 2.3. After 5 days of co-culture, the cells were transferred to 24-well plates. Half of the wells were maintained in regular complete medium, while the other half were switched to osteogenic induction medium (complete medium supplemented with 1 mM Dex, 10 mM ascorbic acid, and 1 M β-glycerophosphate sodium). On day 7, alkaline phosphatase (ALP) activity was detected using the BCIP/NBT ALP detection kit (Beyotime, China). On day 14, calcium deposition on EO-MTs was stained with Alizarin Red S (ARS). After thorough staining, the staining solution was washed off, and the ARS-stained calcium deposits were dissolved in 10% w/v cetylpyridinium chloride. The absorbance was then measured at a wavelength of 562 nm.

For C518 cells of the same passage, cells were harvested by trypsinization and seeded into six-well plates. Half of the wells were cultured under normal conditions, while the other half were supplemented with additional PMs. The plates were then incubated on an orbital shaker. On day 4, culture supernatants were collected, and the secreted glycosaminoglycan (GAG) content was measured using an enzyme-linked immunosorbent assay (ELISA) kit. For C-MTs, at different time points (days 1, 4, and 7) of co-culture, 2 mL aliquots were collected from the co-culture system under mixed conditions. Of these aliquots, 1 mL was used for GAG content detection, while the remaining 1 mL was used for DNA content assay. GAG content was then normalized to DNA content.

2.4. Preparation and characterization of microtissue–gelatin methacryloyl composite bioink

For the modification of gelatin with methacrylic anhydride and subsequent processing, gelatin was added to carbonate buffer (0.25 M, pH = 9.0) and heated at 50°C to facilitate dissolution. Once the solution became clear with no visible undissolved gelatin particles, methacrylic anhydride was slowly added, and the reaction was allowed to proceed under continuous stirring in the dark. During the reaction, the pH was maintained using 1 M NaOH. Following the reaction, the solution was immediately transferred to a preheated dialysis membrane (molecular weight cutoff: 8–14 kDa) while still hot for dialysis. Dialysis was performed with water changes three times daily for one week. After dialysis, the solution was frozen overnight in a −80°C freezer and subsequently lyophilized for 48 h, yielding a spongy sample. The sample was then stored dry at −20°C.

An Avance III 500 MHz spectrometer (Bruker, Switzerland) was used to acquire ^{1}H nuclear magnetic resonance (NMR) spectra at room temperature. Samples were dissolved in D_2O (10 mg/mL) and measured in a 5 mm NMR tube. GelMA was dissolved in PBS buffer at 50°C under gentle stirring to prepare a 10% w/v solution. Then, 0.25% w/v lithium phenyl-2,4,6-trimethylbenzoylphosphinate was incorporated to form the GelMA bioink. For FESEM observation, 1 mL of bioink was crosslinked under blue light for 30 s in a mold. The resulting hydrogel was frozen in liquid nitrogen, lyophilized for 48 h, snap-fractured in liquid nitrogen, and sputter-coated with gold before imaging. To assess swelling behavior, PMs were blended into the GelMA bioink and crosslinked. After demolding, samples were rinsed with PBS (pH 7.4) and blotted to remove excess liquid. The initial dry weight was recorded. Samples were immersed in 20 mL PBS at 37°C under shaking (50 rpm). At specified intervals (1–24 h), samples were removed, blotted, and weighed. Swelling equilibrium was defined as a weight change ≤5% between two consecutive points. The swelling ratio and moisture ratio were calculated accordingly. Rheological properties were characterized using a dynamic shear rheometer Discovery HR-1 (TA Instruments, US) with a 50 mm parallel-plate geometry (1 mm gap). Both uncrosslinked (PM/GelMA mixture with photoinitiator, degassed) and crosslinked (1-mm-thick discs, photocured) samples were tested. Shear viscosity was measured at room temperature from 0 to 1000 s^{-1}. Temperature-dependent viscosity and moduli (G' and G") were recorded during cooling from 40°C to 0°C at 5°C/min.

2.5. Construction of biomimetic osteochondral tissue model

The mixture of C-MTs or EO-MTs and GelMA hydrogel was layer-printed by an extruded 3D bioprinter to construct a biomimetic osteochondral tissue model. First, EO-MT–GelMA hydrogel composite (50 microtissue/mL) was printed in six-well plates and cured using blue light irradiation for 10 s. The C-MT–hydrogel composite (50 microtissue/mL) was then printed on the EO-MT layer and cured using blue light irradiation. Then, 1 mL of the complete medium was added and placed in an incubator. Meanwhile, MT/GelMA bioink was directly added into sterilized silicone molds, photocrosslinked with blue light,

demolded, and then transferred to six-well plates for culture as the casting group. On days 1, 4, and 7, cell viability of both the casting group and the scaffold group was assessed using the CCK-8 assay. On day 14, the scaffolds were retrieved, washed with PBS to remove residual medium, and their structural integrity was observed. Additionally, on day 14, the scaffolds were stained using the BCIP/NBT ALP chromogenic kit; on day 21, calcium deposition on the scaffolds was stained with ARS.

For cellular tracking, C-MTs and EO-MTs were labeled with Qtracker®655 and Qtracker®525, respectively. The labeled MTs were then mixed with GelMA hydrogel and printed under light-protected conditions, followed by blue light-induced photocrosslinking. The constructs were transferred to a cell culture incubator for subsequent culture, and all subsequent procedures were performed under dark conditions. On days 7 and 14, the interface region between the osseous layer and cartilaginous layer was observed using CLSM.

2.6. Lipopolysaccharide-induced osteoarthritis model

Medium containing LPS at different concentrations (0, 0.01, 0.5, 1, and 10 μg/mL) was added to cultured chondrocytes for 48 h, and the cell viability was investigated using the CCK-8 assay. After the biomimetic osteochondral tissue model was constructed, LPS (0.5 μg/mL) was added to the culture medium for 6, 24, and 48 h to induce OA. At various time points, the supernatants were collected, and the levels of TNF-α and IL-1β were then detected using respective ELISA assay kits (LunChangShuoBiotech, China). In addition, Dic, Dex, and Cur were used as the drug model to treat OA. Different concentrations of Dic (75, 100, and 125 μM), Dex (1.5, 3, and 4.5 μM), and Cur (30, 40, and 50 μM) were added to the culture medium. After 48 h of incubation, cell viability was assessed using the CCK-8 assay. Cur was labeled with FITC, added to the cells, and incubated for a certain period of time. Then, the cells were fixed with 4% paraformaldehyde, nuclear stained with DAPI, and observed using CLSM imaging. The designed biomimetic joint tissue was treated with LPS for 48 h, and was then added Dic, Dex, or Cur solution for incubation over 48 h. The contents of inflammatory cytokines TNF-α, IL-1β, IL-6, and IL-10 in the supernatant were measured using ELISA kits. All the assays were performed in triplicate, and the data were representative of three experiments.

2.7. Statistical analysis

Data were analyzed using Origin 2021 (Origin Lab, US). All experimental data displayed as mean ± standard deviation (SD) were assessed using the unpaired Student's *t*-test and analysis of variance with post hoc test using Tukey's honestly significant difference (HSD) method, and $p < 0.05$ was considered statistically significant.

3. Results and discussion

3.1. Characterization of polymeric microarchitectures

This study employed the microfluidic technique to fabricate PLGA-based porous PMs. The gelatin was distributed in the PLGA droplets as a porogen and then corroded using hot water. Notably, the FESEM images (Figure 2A & B) showed that the microfluidic techniques resulted in monodisperse PMs with a uniform diameter of 450–550 μm and a pore size distribution in the range of 20–50 μm (Figure 2D & E). In addition, the cross-sectional view of the PMs presented interconnected windows (Figure 2C), which could substantially facilitate the transportation of nutrients and oxygen. These results were in agreement with the reported literature, in which PMs with a diameter of 250–700 μm could retain the viability of cells cultured for 3–14 days due to their significant proliferation ability, attributing to the interconnected pores of 20–70 μm.[47,48]

The designed PMs were further systematically characterized using various techniques and compared with the raw PLGA material (Figure S1). The results showed that no structural changes occurred during the preparation process. The PMs exhibited a uniform size with porous structure and good physicochemical characteristics—potentially an optimal platform for cell growth.

Notably, the degradability attribute of the biomaterials is equally important to exploring the characterization and performance efficacy. To this end, PMs were placed in PBS and incubated for seven weeks to investigate their degradation properties. As presented in Figure S2, although PLGA was gradually degraded, the porous structure of the PMs remained intact for several weeks, suggesting them as the most suitable carrier for cells, while the slow degradation of PMs favored biomaterial absorption and tissue formation.[49–51] In addition, protein adsorption effects were used to explore cell adhesion effects on the surface of the PMs by exposing the PMs to serum proteins and evaluating them using the Bradford protein assay following the manufacturer's instructions. The results showed that the adsorption kinetics of the proteins were approximately 1.40×10^{-2} mg/PM for 30 min, followed by equilibrium (Figure S3). Collectively, the characterizations, degradability, and protein adsorption efficacy could substantially reflect the cell adhesion ability of the designed PMs, indicating their potential ability for tissue regeneration.[50,52]

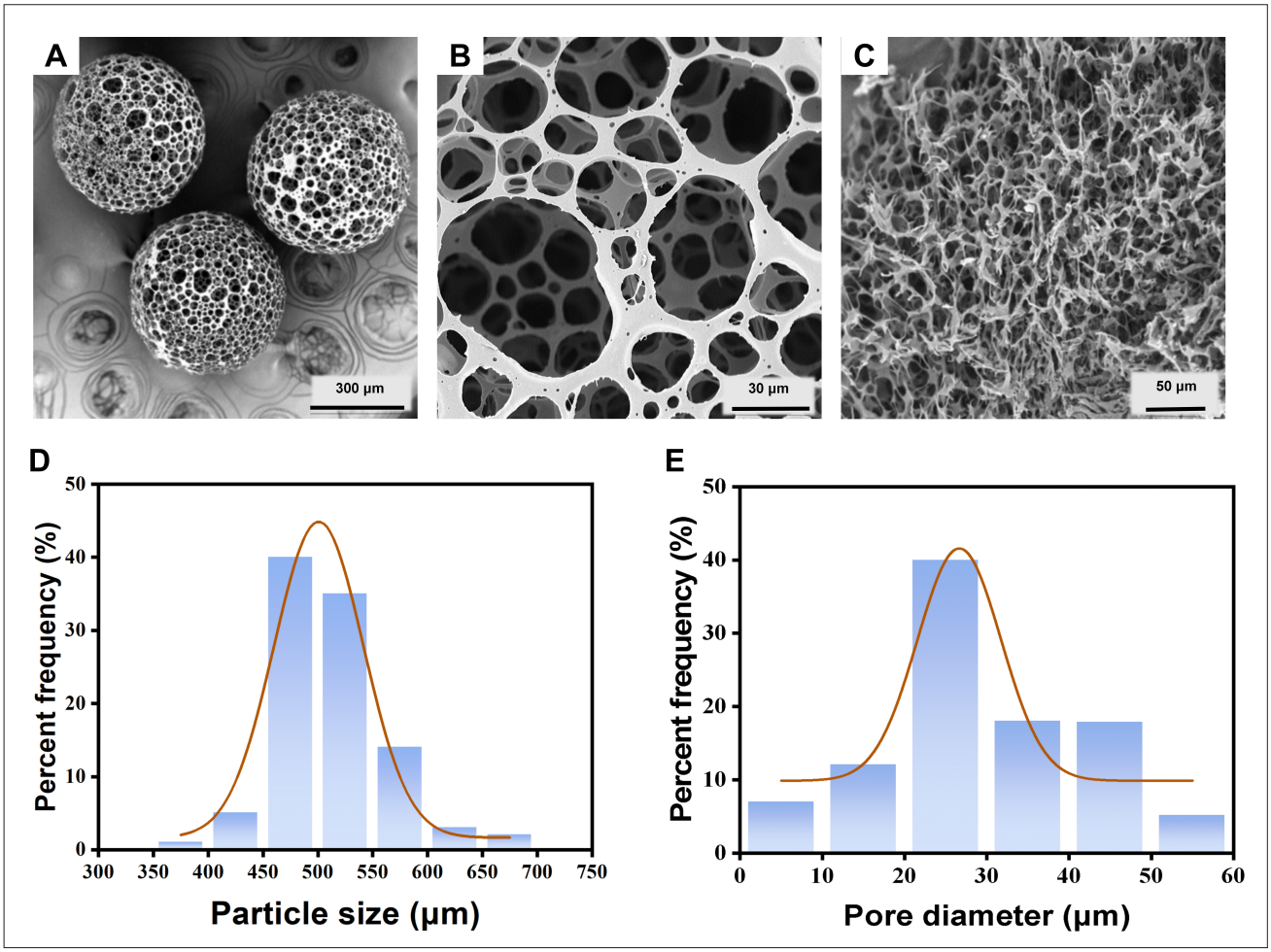

Figure 2. Characterizations of the polymeric microarchitectures. (A & B) Scanning electron microscopy images of the particles. Scale bars: (A) 300 μm, (B) 30 μm; magnification: (A) 200×, (B) 700×. (C) Cross-sectional view. Scale bar: 50 μm; magnification: 900×. (D) Particle size distribution. (E) Pore diameter distribution.

3.2. Preparation and characterization of cartilaginous cellular microtissues and endothelial osteoblastic microtissues

Among several constituents, chondrocytes and subchondral osteoblasts are key components of articular joints. Within these joints, blood vessels are distributed in the subchondral bone, where endothelial cells play a pivotal role in bone development and in the repair of articular body joints.[53] Considering these aspects, MC3T3-E1 cells and MAECs were co-cultured in the PMs to simulate subchondral bone tissues. Different concentrations of PM suspension were prepared to treat the cells. The live and dead staining fluorescence images at 24 h showed that almost no dead cells existed, with a high cell survival rate, indicating that the PM suspensions had no obvious toxicity to the cells at this time (Figure 3A). Furthermore, the CCK-8 assay was used to detect the cytotoxicity of the PM suspension, and the results showed that high cell viability was still observed at the concentration of 1 mg/mL for 72 h (Figure 3B & C).

C-MTs and EO-MTs, both static and dynamic cultivation methods were employed. The adhesion and growth of cells on the PMs were determined through nuclear staining and the measurement of cell proliferation, respectively. It was evident that the MC3T3-E1 cells and MAECs presented excellent proliferation efficacy with the increased cell numbers in the initial 5 days, potentially attributing to the biocompatibility of the PMs (Figure 4A). Additionally, the highly open and porous microstructure facilitates cellular penetration into the PMs while enabling efficient substance exchange to meet the nutritional requirements of cells within the PMs, thereby promoting cell filling within its interior. Similarly, C-MTs also presented excellent proliferation efficacy of chondrocytes in the PMs (Figure 4A), demonstrating that all three cell

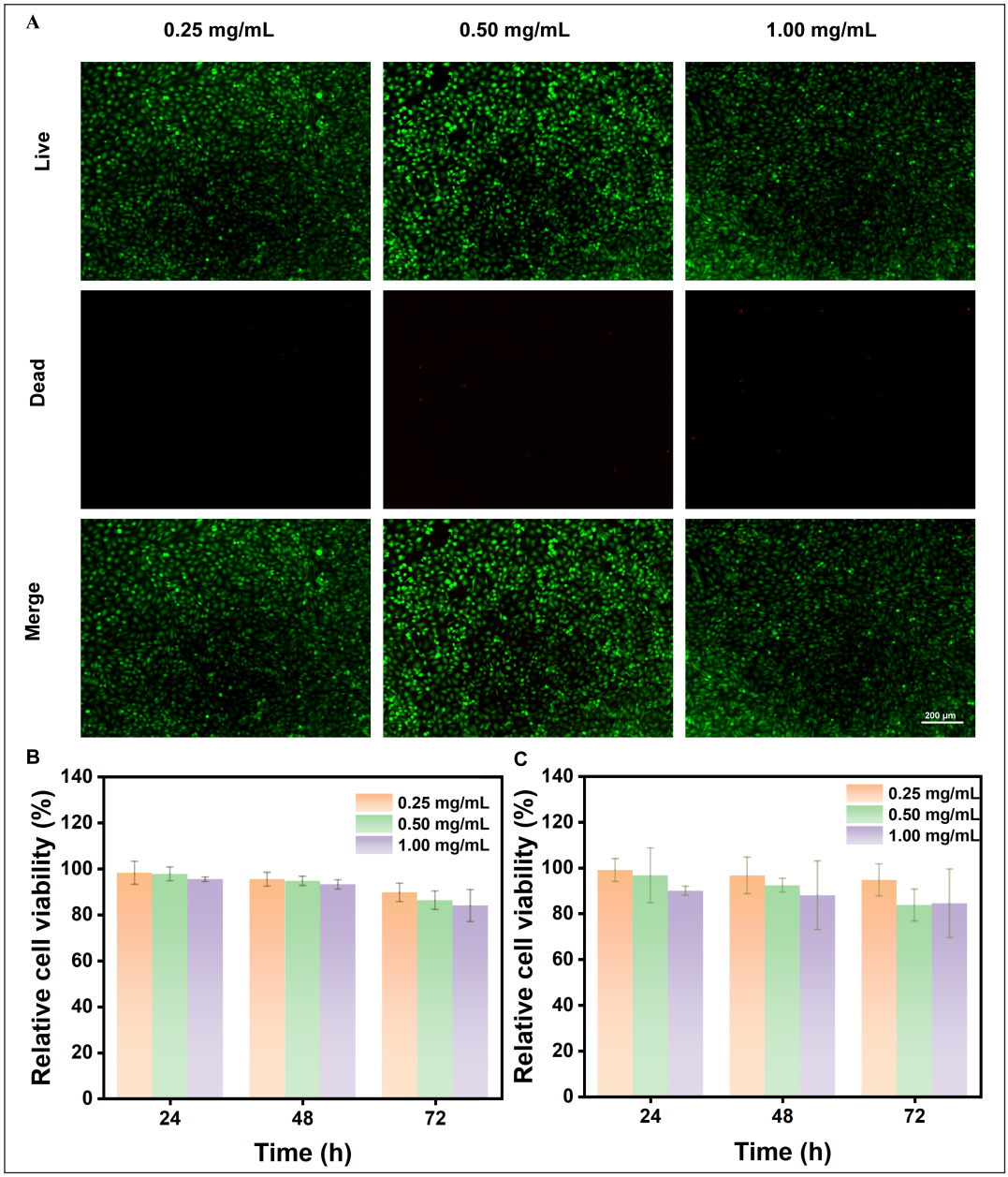

Figure 3. The biocompatibility of polymeric-microarchitecture suspensions. (A) Fluorescence images of the live and dead staining of cells treated with different concentrations of suspensions for 24 h (green: live; red: dead). Scale bar: 200 μm; magnification: 40×. Cell cytotoxicity of (B) MC3T3-E1 (n = 3) and (C) C518 (n = 3) under different suspension concentrations and exposure times was analyzed using the cell counting kit-8 assay.

types could grow well in the PMs. Notably, comparative analysis revealed that cells in MTs prepared under dynamic culture exhibited slightly higher proliferation than those in static culture, attributable to enhanced nutrient, oxygen, and waste transport.[33]

In addition, the adhesion and proliferation efficiencies of cells in PMs were measured quantitatively using the cell counting and CCK-8 analyses, respectively. The results showed that the PMs possessed excellent cell adhesion ability. In EO-MTs under static culture, the average adhesion rate of MC3T3-E1 cells and MAECs was 6.0% at 3 h compared to the inoculated cell numbers, which subsequently increased to 10.5% at 9 h and 28.6% at 24 h (Figure 4B). Interestingly, the cell adhesion rate in the dynamic culture method was 33.1% at 24 h, markedly higher than that of the static culturing method. Although there exists a slight difference, both cell culturing modes

presented excellent adhesion efficacies. Meanwhile, cell proliferation in EO-MTs showed that the relative viability rate of harbored cells nearly doubled from day 1 to day 7 under static culture, indicating that the 3D microenvironment of PMs was optimal for cell growth (Figure 4C). Similarly, CLSM observations (Figure 4A) showed a significant increase in dynamically cultured C518 chondrocytes after initial adhesion within the polymer structure, with cells maintaining a steady growth state in PMs (Figure 4D & E). Notably, C518 chondrocytes showed proliferation and infiltration patterns similar to those of MAECs and MC3T3-E1 cells, with a 24 h adhesion rate of 58.2% under dynamic culture, exceeding that achieved under static culture.

In normal subchondral bone, endothelial cells are essential for intercellular signaling, angiogenesis, and osteogenesis. Hence, the strategy to prepare EO-MTs apparently mimics subchondral tissues. Co-culturing endothelial cells with osteocytes is the most direct approach to establishing the vascular function of supplying nutrients and metabolite excretion for constructing bone tissue models. Accordingly, MAECs were co-cultured with MC3T3-E1 cells in PMs, mimicking native vascularized bone tissues. To investigate cell distribution in EO-MTs, the osteoblasts and the endothelial cells were fluorescently labeled using Qtracker®655 and Qtracker®525, respectively. Although angiogenic sprouting and vascular lumen formation were rarely seen, CLSM imaging confirmed that both MAECs and MC3T3-E1 cells were distributed in the MTs and maintained high viability (Figure 5A). Together, the co-culture of MC3T3-E1/MAEC in PMs produced complex tissues with considerable cell–cell communications, indicating the establishment of a vascularized bone-like microenvironment. In the cultured C-MTs, cartilage-specific proteins, including aggrecan, collagen I, and collagen II, were detected (Figure 5B), indicating robust chondrocyte proliferation within the carriers. In addition, HE staining was performed to better visualize cell distributions on the PMs. It was evident that the tissues with dense cell density and orderly arrangement were formed, while prolonged culture induced scaffold morphology changes due to the aggregation of individual PM architectures (Figure 5C). Furthermore, in our previous study,[30] the bioefficacy of MTs constructed using cell-laden PLGA-based PMs was demonstrated, as cells released significantly higher levels of essential proteins, including albumin and multidrug resistance proteins, compared to 2D static culture. Taken together, these findings suggest that the designed PMs provide abundant adhesion sites, support high cell viability, and sustain essential cell functions.

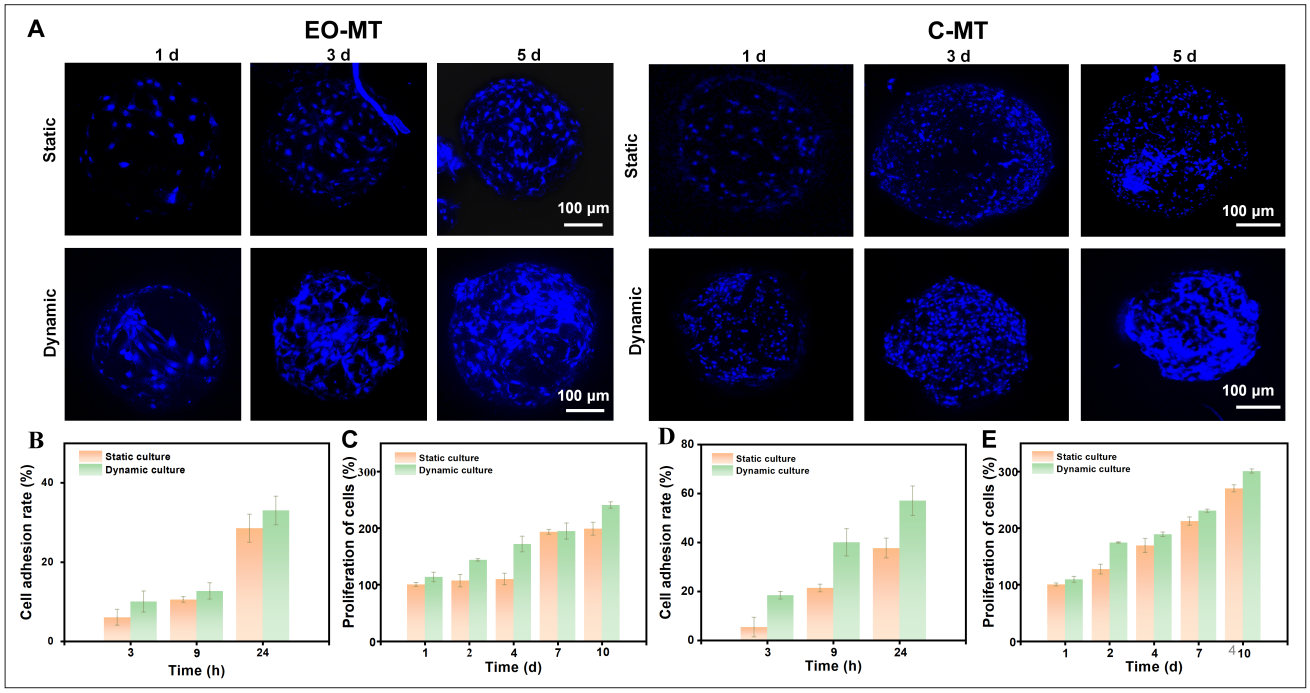

Figure 4. Co-culture of polymeric microarchitectures and endothelial osteoblastic microtissues (EO-MTs) or cartilaginous cellular microtissues (C-MTs). (A) Confocal laser scanning microscopy images of EO-MTs and C-MTs cultured for different times (blue: DAPI). Scale bar: 100 μm; magnification: 40×. Quantification of cell adhesion and proliferation in (B & C) EO-MTs and (D & E) C-MTs under static or dynamic culture modes (n = 3).

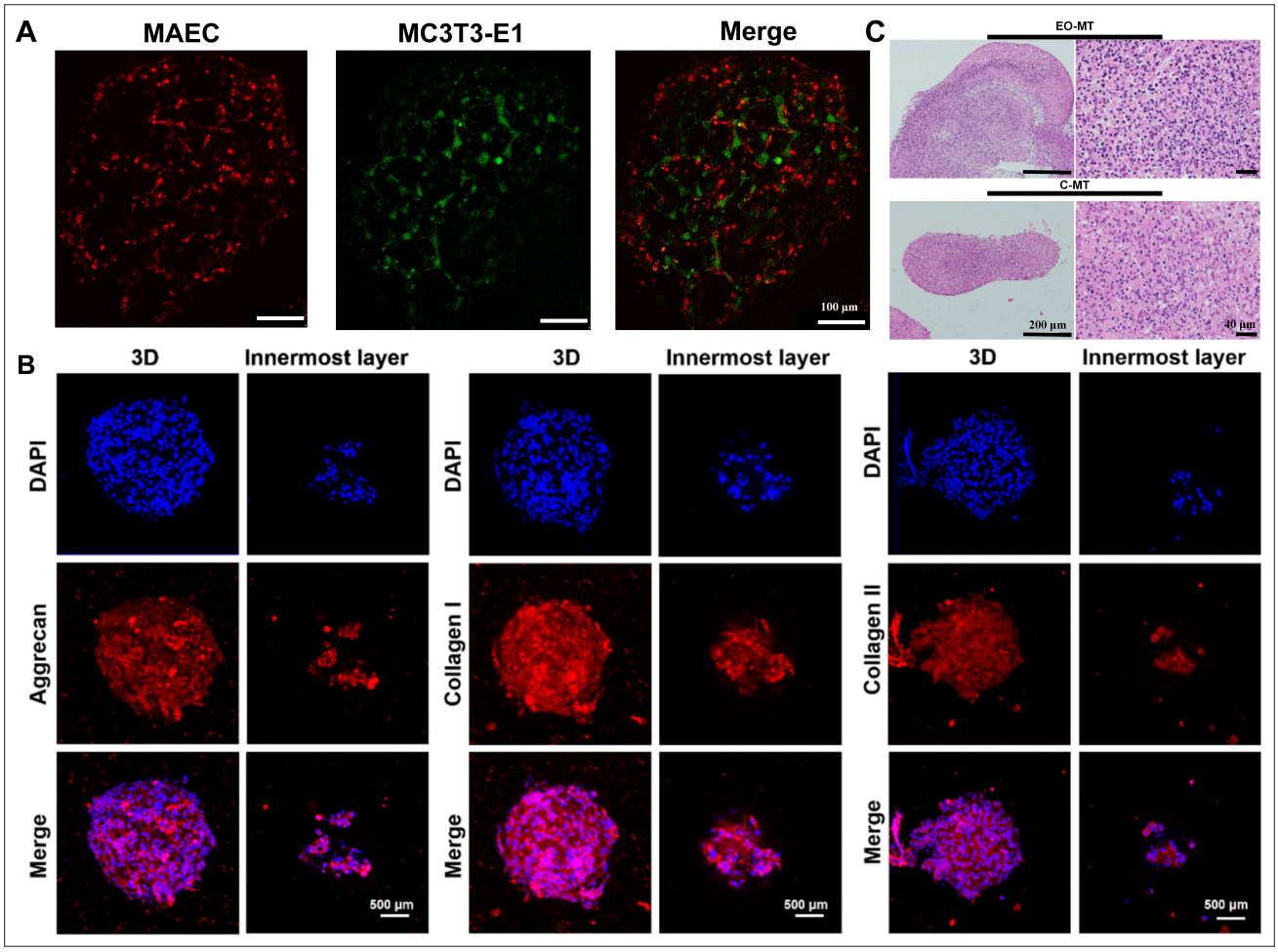

Figure 5. CLSM imaging. (A) CLSM of MAECs and MC3T3-E1 cells in EO-MTs. Scale bar: 100 μm; magnification: 20×. (B) CLSM of aggrecan, collagen I, and collagen II in C-MTs. Scale bar: 500 μm; magnification: 10×. (C) Hematoxylin and eosin staining of EO-MTs and C-MTs. Scale bar: 200 or 40 μm; magnification: 40× and 100× Abbreviations: C-MT, cartilaginous cellular microtissue; EO-MT, endothelial osteoblastic microtissue; MAEC, mouse aorta endothelial cell; CLSM, confocal laser scanning microscopy.

To better recapitulate native cartilage and subchondral bone microenvironments, the functionalized culture of the prepared EO-MTs and C-MTs was performed. For EO-MTs, osteogenic induction medium was formulated by supplementing complete medium with osteogenic growth factors, including Dex, ascorbic acid, and β-glycerophosphate sodium, followed by long-term culture. ALP, a key and classical biomarker for osteoblast activity and bone formation, directly reflects osteoblast maturation and functional status. It plays a crucial role in bone matrix mineralization; its expression is significantly upregulated when osteoblasts transition from the proliferative phase to the mature differentiation phase. On day 7, quantitative analysis of ALP activity in EO-MTs using an ALP assay kit revealed that the osteogenic induction group exhibited significantly higher activity (0.141 μM) compared to the non-induced blank group (0.107 μM), indicating that osteoblasts adhering to and proliferating on EO-MTs had entered an active bone-forming phase (Figure 6A). Notably, increased ALP activity does not necessarily indicate extensive mineralized bone formation; thus, on day 14, ARS staining was performed to visualize calcium nodules on EO-MTs (Figure S4), followed by quantitative analysis via dissolution with 10% w/v cetylpyridinium chloride (Figure 6B). The results showed significantly higher calcium deposition in the osteogenic induction group than in the blank group, confirming calcium salt deposition and indicating mineralized bone formation. Through ALP and ARS stainings, markers of early and late osteogenesis, respectively, mutually validate the successful osteogenic functionalization of EO-MTs. These findings align with the regulatory role of Runt-related transcription factor 2 (RunX2), the master transcription factor of osteogenesis, where ALP upregulation and ARS-positive

mineralization represent the terminal events of RunX2-mediated signaling cascade activation.

For C-MTs, GAG, a critical component of chondrocyte ECM, serves as a direct indicator of chondrogenic MT maturity and quality. On day 4 of co-culture, GAG content in supernatants (Figure 6C) showed that 2D-cultured cells exhibited higher GAG levels (106.8 μg/mL) than 3D-co-cultured cells on PMs (49.5 μg/mL). This can be attributed to the fact that 3D PMs provide abundant attachment sites for secreted GAG, which gradually deposit on the scaffold to form ECM, whereas 2D-cultured GAG diffuses freely into the medium. Additionally, for 3D-co-cultured C-MTs, deposited GAG was detected at different time points and normalized to DNA content (Figure 6D), revealing that chondrocytes gradually adapted to the microenvironment, activated the synthetic phenotype, and initiated GAG and proteoglycan synthesis over time, indicating MT formation and favorable cellular functionality. This progressive GAG accumulation corresponds to the terminal output of the SOX-9 signaling cascade, as SOX-9, the central transcription factor for chondrogenesis, directly regulates the expression of GAG-synthesizing enzymes and proteoglycan core proteins. In summary, the functionalized culture of MTs enables improved recapitulation of native cartilage and subchondral bone microenvironments.

3.3. Characterization of microtissue–gelatin-methacryloyl-hydrogel composite bioink

GelMA hydrogels were synthesized via amidation of gelatin amino groups with methacrylic anhydride, as confirmed by ^{1}H NMR analysis. The spectrum showed characteristic peaks of methacrylate vinyl protons (δ = 5.31 and 5.55 ppm) and the attenuation of the amide-associated signal (δ = 2.88 ppm), indicating effective double-bond modification (Figure 7A). GelMA hydrogels exhibited an interconnected porous structure after lyophilization (Figure 7B), favorable for nutrient diffusion and cell infiltration. Subsequently, PM–GelMA composite hydrogels were prepared, and swelling ratio and moisture ratio tests were performed (Figure 7C & D). The results showed that the addition of PMs had no significant effect on the bioink, potentially because the added PMs were already in an equilibrium state; the slight increase observed in the composite group may be attributed to the added MTs increasing the internal space of the overall structure. Mechanical property test results (Figure 7E & F) demonstrated that increasing MT concentration from 0 to 20 mg/mL enhanced hydrogel stiffness, as evidenced by steeper stress–strain curves and a higher compressive modulus. This enhancement can be attributed to PMs acting as rigid fillers that facilitate stress transfer within the gel network. Since matrix stiffness is known to effectively regulate cell behavior—higher stiffness promotes osteogenic differentiation while moderate or lower stiffness favors chondrogenesis[54,55]—these results suggest that adjusting PM incorporation offers a practical strategy for modulating hydrogel stiffness in future studies.

Rheological analysis further confirmed that PMs improved the printability of GelMA bioinks. Both GelMA and PMs/GelMA displayed thermo-responsive gelation, with G' surpassing G" near 15°C (Figure 7G), indicating sol–gel transition unaffected by PM addition. Temperature–viscosity curves further demonstrated the thermal responsiveness of GelMA and PMs/GelMA; however, the initial viscosity of PM-containing inks was significantly higher than that of pure GelMA (Figure 7H). This may be due to the increased internal friction of particle–polymer interactions and the complexity of the microstructure. This property is advantageous for 3D bioprinting, as higher static viscosity enhances shape fidelity. Importantly, shear-thinning behavior was preserved (Figure 7I), satisfying the extrusion printing requirement of high viscosity at rest and low viscosity under shear. In conclusion, the incorporation of PMs not only achieves effective regulation of the swelling behavior and mechanical strength of GelMA hydrogels but

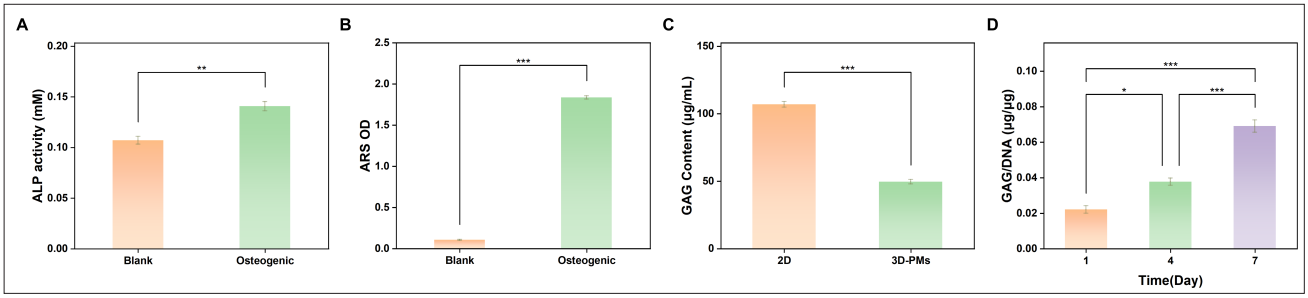

Figure 6. Functional characterization of microtissues during culture. (A) ALP activity of EO-MTs at day 7 of osteogenic induction culture (n = 3). (B) Quantitative analysis of ARS staining for calcium deposition in EO-MTs at day 14 of osteogenic induction (n = 3). (C) GAG content in the supernatants of C518 cells cultured for 4 days under different conditions (n = 3). (D) Changes in GAG content of C-MTs at different culture time points (n = 3). Notes: *p < 0.05, **p < 0.01, ***p < 0.001. Abbreviations: ALP, alkaline phosphatase; ARS: Alizarin Red S; C-MT, cartilaginous cellular microtissue; EO-MT, endothelial osteoblastic microtissue; GAG, glycosaminoglycan; OD, optical density; PM, polymeric microarchitecture.

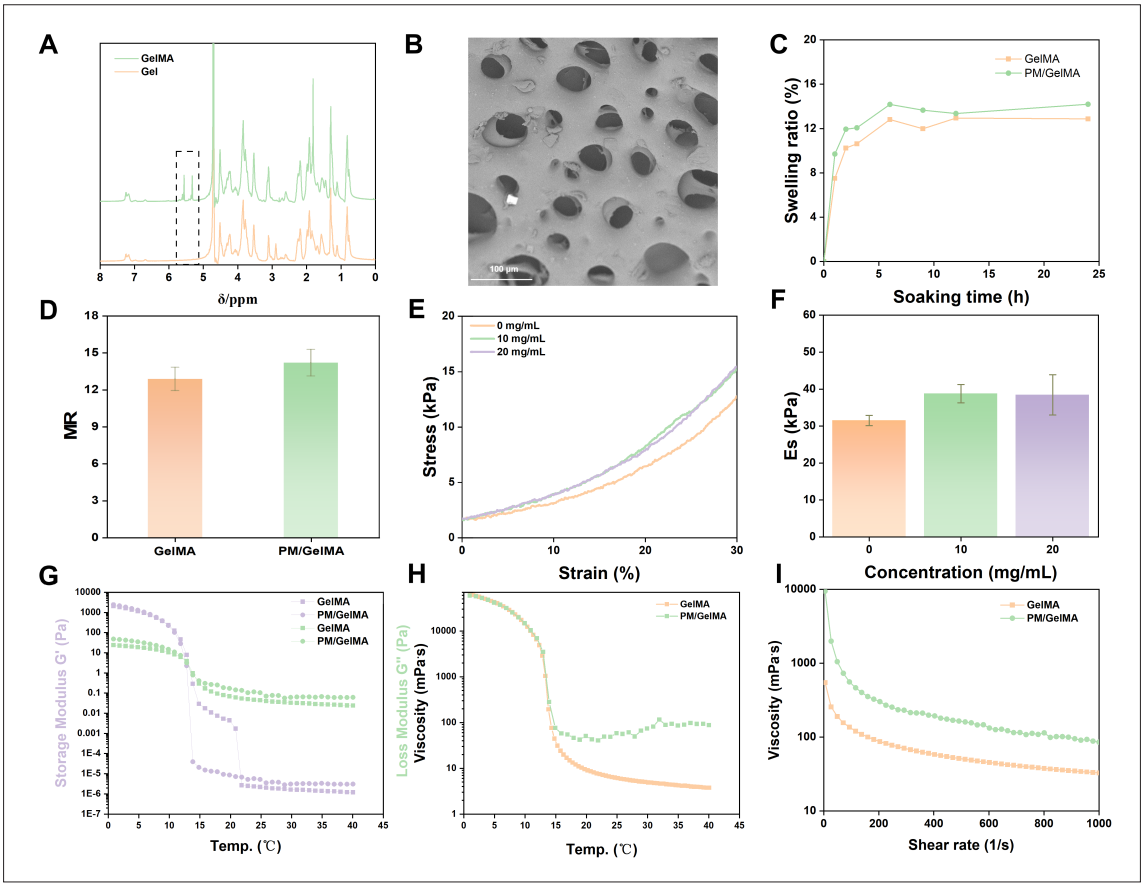

Figure 7. Physicochemical characterization of bioink. (A) ^{1}H NMR spectra of gelatin and GelMA. (B) Scanning electron microscopy image of photocrosslinked GelMA. Scale bar: 100 μm; magnification: 600×. (C) Swelling ratio. (D) MR. (E) Stress–strain curves. (F) Compressive modulus (Es). (G) Storage modulus (G') and loss modulus (G"). (H) Temperature–viscosity curves. (I) Shear rate–viscosity curves of PM/GelMA composite bioink. Abbreviations: GelMA, gelatin methacryloyl; NMR, nuclear magnetic resonance; PM, polymeric microarchitecture; MR, moisture ratio.

also endows them with good printability by optimizing rheological properties, laying the experimental foundation for the application of this composite bioink in the field of bone/cartilage tissue engineering.

PMs were co-cultured with different cell types to generate corresponding MTs, which were then subjected to functionalized culture. Subsequently, the MTs were uniformly mixed with GelMA for 3D bioprinting. To intuitively demonstrate the advantages of 3D printing, mold-cast and 3D-printed MT/GelMA constructs were prepared separately (Figure 8A). After culturing for different time periods, cell viability was assessed using the CCK-8 assay (Figure 8B). The results showed that the 3D-bioprinted scaffold group exhibited significantly enhanced cell proliferation capacity compared to the mold-cast group. This could be attributed to the fact that mold-cast solid cylindrical hydrogels typically have a dense structure (or rely solely on the material's intrinsic microporosity), whereas 3D-printed scaffolds can form regular and interconnected macroporous channel networks through parameter design (e.g., layer height, pore size, and porosity), thereby providing superior mass transfer capacity, including the transport of oxygen and nutrients as well as the removal of metabolic waste. Furthermore, the mechanical microenvironment of 3D-printed scaffolds is better suited for cell proliferation. Mold-cast solid cylindrical hydrogels generally have high and uniformly distributed overall mechanical strength, while the porous structure of 3D-printed scaffolds allows the regulation of local stiffness through design, more closely mimicking the mechanical heterogeneity of native tissues. The channel structure of the scaffold permits local elastic deformation, avoiding "mechanical compression" of cells caused by excessive overall rigidity of solid cylinders, while providing moderate mechanical stimulation. Meanwhile, the porous network of 3D-printed scaffolds facilitates cells to secrete their own ECM components (e.g., collagen and fibronectin) and undergo matrix remodeling, forming a "cell–matrix"

positive feedback loop that further supports proliferation. In contrast, the dense structure of solid cylinders limits the active-matrix remodeling capacity of cells.

To better recapitulate the osteochondral model, the scaffolds were continuously subjected to functionalized culture. After one week of culture, the scaffold maintained good structural integrity (Figure 8Ci). On day 14, ALP activity in the bone layer of the scaffold was characterized using an ALP chromogenic kit (Figure 8Cii), and on day 21, the mineralization level of the bone layer was characterized via ARS staining (Figure 8Ciii). The results indicate that the scaffold exhibited favorable osteogenic capacity.

Subsequently, EO-MTs and C-MTs were fluorescently labeled separately and then subjected to bioprinting. After culturing for different time periods, the scaffolds were observed via CLSM. The primary focus was on the interface region between the EO-MT layer and the C-MT layer. On day 7 of culture (Figure 8Di), distinct upper and lower cell layers were observed. In addition, faint red fluorescence was detected at the bottom of the green-fluorescent C-MT layer. On day 14 (Figure 8Dii), significant overlap between red and green fluorescence was observed. These results indicate that with the extension of culture time, the bone layer represented by EO-MTs and the cartilage layer represented by C-MTs exhibit gradually enhanced crosstalk, suggesting that the cartilage and bone layers may eventually achieve functional integration.

3.4. Biological performance of osteoarthritis model

In recent times, 3D bioprinting technology has garnered enormous attention to fabricate engineered living systems for better health.[56] By applying this innovative technology, a microarchitecture-based hierarchical osteochondral model was fabricated, mimicking the osteochondral microenvironment *in vivo*. The 3D model was constructed using the MT–GelMA composite bioink (Figure 8A). GelMA was selected as it provides a bionic interface for

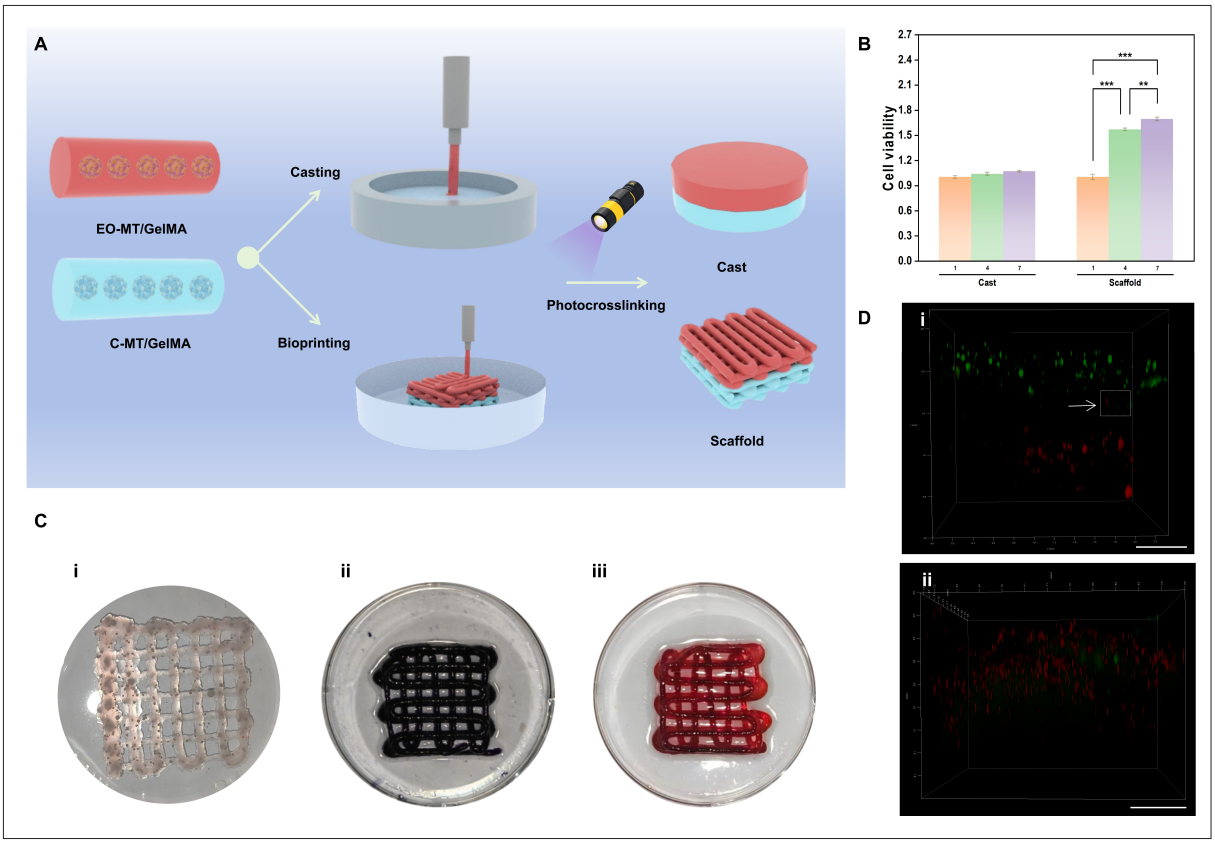

Figure 8. Bioprinting and characterization of MT/GelMA composite bioink. (A) Schematic representation of the osteochondral model constructed by 3D bioprinting and direct casting. (B) Cell viability of the casting group and scaffold group at different time points ($n = 3$). (C) Macroscopic images of the scaffold: (i) Macroscopic morphology after one week of culture; (ii) ALP staining image after 14 days of culture; and (iii) ARS staining image after 21 days of culture. (D) Confocal laser scanning microscopy images of the scaffold at different culture time points: (i) Day 7 and (ii) Day 14 (green: C-MTs, red: EO-MTs). Scale bar: 500 μm; magnification: 10×. Notes: $^{**}p < 0.01$, $^{***}p < 0.001$. Abbreviations: ALP, alkaline phosphatase; ARS: Alizarin Red S; C-MT, cartilaginous cellular microtissue; EO-MT, endothelial osteoblastic microtissue; GelMA, gelatin methacryloyl; MT, microtissue.

cartilages and bone tissues, facilitating the transportation of nutrients due to the porosity of hydrogel networks. The 3D model was completely immersed in the medium for continuous culture, and then LPS was added to induce OA. Dic, Dex, and Cur were selected for drug screening, and the production and improvement of inflammation were verified by detecting the levels of anti-inflammatory and pro-inflammatory factors (Figure 9A).

To elucidate the drug screening efficacy of the designed 3D osteochondral model, herein, LPS-induced inflammation was further applied to the pre-designed 3D chondrocyte model *in vitro*. LPS, a component of bacterial membrane, has been extensively used to establish an inflammatory model as it stimulates the release of inflammatory cytokines, including IL-8, IL-6, and IL-1β.[57] The *in vitro* chondrocyte model of LPS-induced

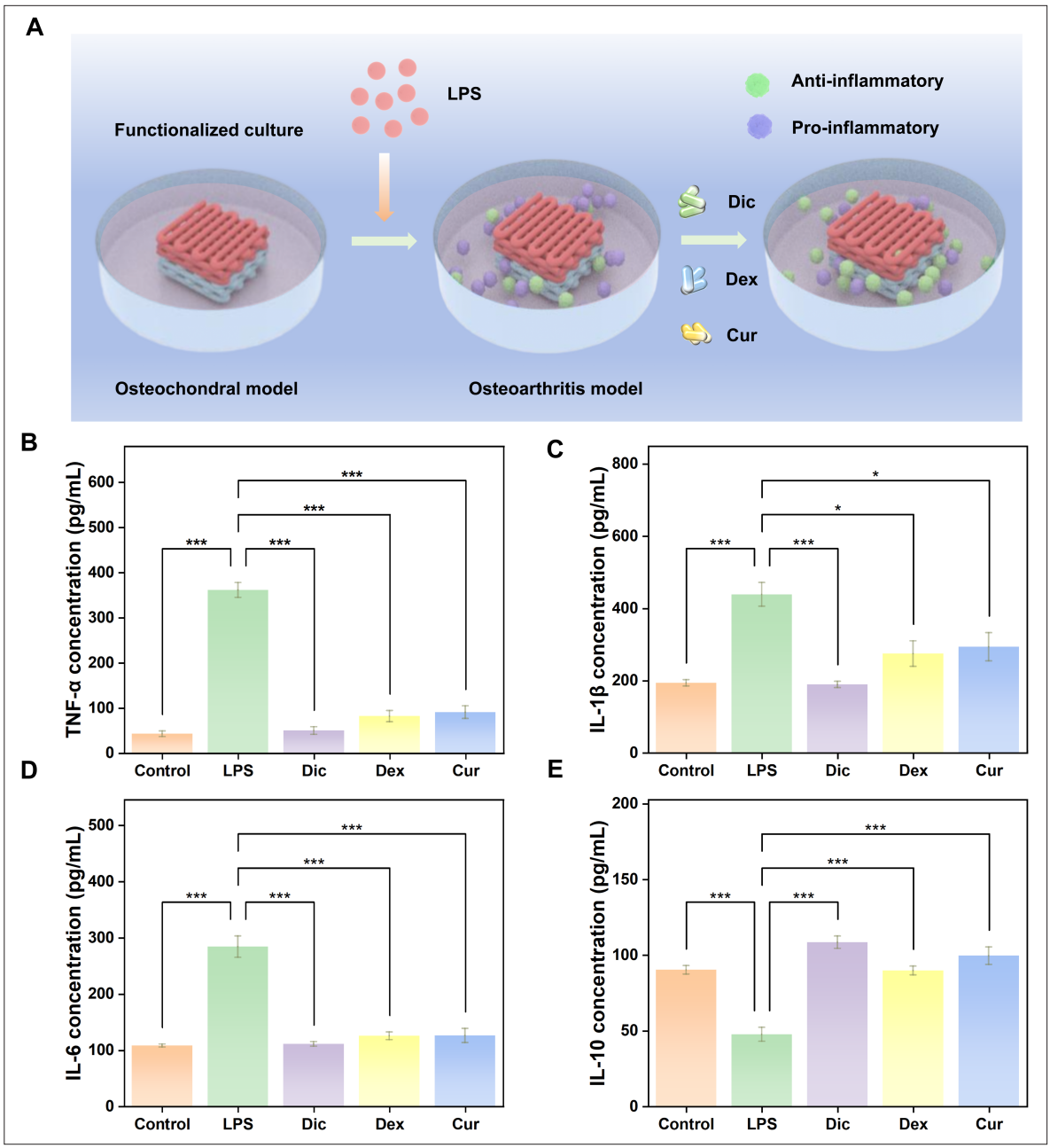

Figure 9. Bioprinting of microtissue bioinks. (A) Schematic diagram of the OA model constructed for drug screening. The effects of drug treatment on (B) TNF-α, (C) IL-1β, (D) IL-6, and (E) IL-10 concentrations ($n = 3$). Notes: $^{*}p < 0.05$, $^{***}p < 0.001$). Abbreviations: Cur, curcumin; Dex, dexamethasone; Dic, diclofenac; LPS, lipopolysaccharide; TNF-α, tumor necrosis factor-alpha; IL, interleukin; OA, osteoarthritis.

inflammation has been widely reported, showing that the LPS treatment could promote the production of IL-1β and TNF-α in chondrocytes.[58–60] No significant effect on cell viability was detected even when the concentration of LPS reached 1 μg/mL (Figure S5). The next step involved the utilization of LPS to induce the secretion of pro-inflammatory cytokines IL-1β and TNF-α in the OA model for a duration exceeding 48 h. Subsequently, ELISA was employed to measure the levels of LPS-induced IL-1β and TNF-α in the supernatant of the biomimetic osteochondral model (Figure S6). LPS treatment resulted in a 25.1% increase in IL-1β released in the OA model after exposure to 0.5 μg/mL LPS for 48 h, compared to that from the saline-treated group. Similarly, the TNF-α expression was also markedly increased by 29.9% at 48 h following LPS treatment. The secretion of inflammatory cytokines appeared to increase over time, likely due to the interaction between osteochondral cells and LPS, which stimulated further cytokine release. These inflammatory markers are implicated in cartilage inflammation and chondrocyte apoptosis during the development and progression of OA.[60]

To further investigate the performance of the OA model, Dic, Dex, and Cur were tested in the LPS-induced OA model. Dic is an NSAID, Dex is a glucocorticoid, and Cur is a natural polyphenolic compound, each exerting distinct therapeutic mechanisms in OA treatment.[43–45] The CCK-8 assay was used to evaluate the effects of different concentrations of Dic, Dex, or Cur on cell viability over 48 h. Cellular uptake experiments showed that Cur completely entered the cell interior within 4 h (Figure S7). Dic, Dex, or Cur treatment significantly reduced the expression levels of TNF-α, IL-1β, and IL-6 in the LPS-induced model, restoring them to levels close to those in the untreated control group. In parallel, IL-10 expression increased significantly compared to the LPS group, approaching levels in the untreated control group (Figure 9B–D). These findings indicate that the three drugs regulate OA inflammation through a dual mechanism: suppressing pro-inflammatory factors (e.g., TNF-α, IL-1β, and IL-6) while enhancing the anti-inflammatory factor IL-10 via the improvement of the inflammatory microenvironment and immunomodulation. Collectively, these actions restore the balance of the pro-inflammatory–anti-inflammatory cytokine network, approaching the physiological state of the untreated group and demonstrating the effective regulatory effect of the drugs on OA inflammation. Considering the biocompatibility, biodegradability, and performance efficacy of the system against LPS-induced OA, the osteochondral model developed using microfluidics and bioprinting technologies represents a promising platform for screening OA therapeutics.

4. Conclusion

This study established a biomimetic osteochondral model by integrating microfluidics-generated PMs with 3D bioprinting. The PMs provide a biocompatible, microporous framework that supports chondrocyte and endothelial/osteoblast MT formation while preserving cell phenotype and function. Incorporation of PMs into GelMA enables tunable matrix stiffness without compromising printability, facilitating the fabrication of stratified osteochondral constructs. The resulting 3D model sustains long-term cell viability, recapitulates key features of the osteochondral microenvironment, and mimics OA-like inflammation under LPS stimulation by upregulating both pro- and anti-inflammatory cytokines. Importantly, treatment with Dic, Dex, and Cur effectively attenuated the induced inflammatory response, underscoring the platform's translational potential for anti-inflammatory drug screening. Taken together, this biomimetic osteochondral system represents a versatile and physiologically relevant platform for investigating OA pathology, evaluating therapeutic candidates, and advancing osteochondral tissue engineering.

Acknowledgments

None.

Funding

This work was funded by the National Natural Science Foundation of China (grant numbers: 32271410), the Science and Technology Projects in Fujian Province (grant numbers: 2022FX1 and 2023Y4008), the Natural Science Foundation of Fujian Province (grant number: 2022J01297), the Fundamental Research Funds for the Central Universities (grant number: ZQN-1107), and the Program for Innovative Research Team in Science and Technology in Fujian Province, Scientific Research Funds of Huaqiao University (grant number: 24BS132).

Conflict of interest

The authors declare that they have no known competing financial interests or personal relationships that could have influenced the work reported in this paper.

Author contributions

Conceptualization: Yi-Cheng Wang, Xiao-Jie Song, ChaoPing Fu

Funding acquisition: Shi-Bin Wang, Ai-Zheng Chen, Chao-Ping Fu

Investigation: Yi-Cheng Wang, Xiao-Jie Song, Xiao-Chang Lu

Methodology: Yi-Cheng Wang, Xiao-Jie Song
Project administration: Shi-Bin Wang, Ai-Zheng Chen, Chao-Ping Fu
Supervision: Chao-Ping Fu
Visualization: Yi-Cheng Wang, Xiao-Jie Song
Writing–original draft: Yi-Cheng Wang, Xiao-Jie Song
Writing–review & editing: Yue-Wei Li, Zhou-Jiang Chen, Ranjith Kumar Kankala, Chao-Ping Fu

Ethics approval and consent to participate

Not applicable.

Consent for publication

Not applicable.

Availability of data

Additional data and materials not included in the manuscript or supplementary materials are available from the corresponding authors upon reasonable request.

References

1. Bhardwaj N, Singh YP, Mandal BB. Silk fibroin scaffold-based 3D co-culture model formodulation of chondrogenesis without hypertrophy via reciprocal cross-talk and paracrine signaling. *ACS Biomater Sci Eng.* 2019;5(10):5240-5254. doi: 10.1021/acsbiomaterials.9b00573
2. Wang D, Liu W, Venkatesan JK, Madry H, Cucchiarini M. Therapeutic controlled release strategies for human osteoarthritis. *Adv Healthc Mater.* 2024;14(2):e2402737. doi: 10.1002/adhm.202402737
3. Samvelyan HJ, Hughes D, Stevens C, Staines KA. Models of osteoarthritis: relevance and new insights. *Calcif Tissue Int.* 2021;109(3):243-256. doi: 10.1007/s00223-020-00670-x
4. Yessica Eduviges ZC, Martínez-Nava G, Reyes-Hinojosa D, *et al*. Impact of cadmium toxicity on cartilage loss in a 3D in vitro model. *Environ Toxicol Pharmacol*. 2020;74:103307. doi: 10.1016/j.etap.2019.103307
5. Jones G, Winzenberg T. Osteoarthritis: a new short-term treatment option? *Lancet*. 2019;394(10213):1967-1968. doi: 10.1016/s0140-6736(19)32729-1
6. Yang D, Xu J, Xu K, Xu P. Skeletal interoception in osteoarthritis. *Bone Res.* 2024;12(22). doi: 10.1038/s41413-024-00328-6
7. Cowan KJ, Kleinschmidt-Dörr K, Gigout A, *et al*. Translational strategies in drug development for knee osteoarthritis. *Drug Discov Today*. 2020;25(6): 1054-1064. doi: 10.1016/j.drudis.2020.03.015
8. Assi R, Quintiens J, Monteagudo S, Lories RJ. Innovation in targeted intra-articular therapies for osteoarthritis. *Drugs*. 2023;83(8):649-663. doi: 10.1007/s40265-023-01863-y
9. Cao H, Deng S, Chen X, *et al*. An injectable cartilage-coating composite with long-term protection, effective lubrication and chondrocyte nourishment for osteoarthritis treatment. *Acta Biomater.* 2024;179:95-105. doi: 10.1016/j.actbio.2024.03.015
10. Wu M, Zheng K, Li W, *et al*. Nature-inspired strategies for the treatment of osteoarthritis. *Adv Funct Mater.* 2023;34(4):2305603. doi: 10.1002/adfm.202305603
11. Yeung P, Cheng KH, Yan CH, Chan BP. Collagen microsphere based 3D culture system for human osteoarthritis chondrocytes (hOACs). *Sci Rep.* 2019;9(1):12453. doi: 10.1038/s41598-019-47946-3
12. Zou Z, Luo X, Chen Z, Zhang YS, Wen C. Emerging microfluidics-enabled platforms for osteoarthritis management: from benchtop to bedside. *Theranostics*. 2022;12(2):891-909. doi: 10.7150/thno.62685
13. Liu H, Wu X, Liu R, Wang W, Zhang D, Jiang Q. Cartilage-on-a-chip with magneto-mechanical transformation for osteoarthritis recruitment. *Bioact Mater.* 2024; 33:61-68. doi: 10.1016/j.bioactmat.2023.10.030
14. Chapman JH, Ghosh D, Attari S, Ude CC, Laurencin CT. Animal models of osteoarthritis: updated models and outcome measures 2016–2023. *Regen Eng Transl Med.* 2023;10(2):127-146. doi: 10.1007/s40883-023-00309-x
15. Singh YP, Moses JC, Bhardwaj N, Mandal BB. Overcoming the dependence on animal models for osteoarthritis therapeutics – the promises and prospects of in vitro models. *Adv Healthc Mater.* 2021;10(20):2100961. doi: 10.1002/adhm.202100961
16. Zhou M, Lozano N, Wychowaniec JK, *et al*. Graphene oxide: a growth factor delivery carrier to enhance chondrogenic differentiation of human mesenchymal stem cells in 3D hydrogels. *Acta Biomater.* 2019;96:271-280. doi: 10.1016/j.actbio.2019.07.027
17. Ding SL, Zhao XY, Xiong W, *et al*. Cartilage lacuna-inspired microcarriers drive hyaline neocartilage regeneration. *Adv Mater.* 2023;35(30):e2212114. doi: 10.1002/adma.202212114
18. Hwang HS, Kim HA. Chondrocyte apoptosis in the pathogenesis of osteoarthritis. *In. J Mol Sci.* 2015;16(11):26035-26054. doi: 10.3390/ijms161125943
19. Ebata T, Terkawi MA, Kitahara K, *et al*. Noncanonical pyroptosis triggered by macrophage-derived extracellular

vesicles in chondrocytes leading to cartilage catabolism in osteoarthritis. *Arthritis Rheumatol*. 2023;75(8):1358-1369. doi: 10.1002/art.42505

20. Maihemuti A, Zhang H, Lin X, *et al*. 3D-printed fish gelatin scaffolds for cartilage tissue engineering. *Bioact. Mater.* 2023;26:77-87. doi: 10.1016/j.bioactmat.2023.02.007

21. Korpayev S, Kaygusuz G, Şen M, Orhan K, Oto Ç, Karakeçili A. Chitosan/collagen based biomimetic osteochondral tissue constructs: A growth factor-free approach. *Int J Biol Macromol.* 2020;156:681-690. doi: 10.1016/j.ijbiomac.2020.04.109

22. Singh YP, Moses JC, Bandyopadhyay A, Mandal BB. 3D bioprinted silk-based in vitro osteochondral model for osteoarthritis therapeutics. *Adv Healthc Mater.* 2022;11(24):200209. doi: 10.1002/adhm.202200209

23. Salehi S, Brambilla S, Rasponi M, Lopa S, Moretti M. Development of a microfluidic vascularized osteochondral model as a drug testing platform for osteoarthritis. *Adv Healthc Mater.* 2024;13(31):e2402350. doi: 10.1002/adhm.202402350

24. Ong LJY, Sun AR, Wang Z, Lee J, Prasadam I, Toh YC. Localized oxygen control in a microfluidic osteochondral interface model recapitulates bone–cartilage crosstalk during osteoarthritis. *Adv Funct Mater.* 2024;34(28):2315608. doi: 10.1002/adfm.202315608

25. Wei Y, Deng Y, Ma S, *et al*. Local drug delivery systems as therapeutic strategies against periodontitis: a systematic review. *J Control Release*. 2021;333:269-282. doi: 10.1016/j.jconrel.2021.03.041

26. Jo YK, Lee D. Biopolymer microparticles prepared by microfluidics for biomedical applications. *Small*. 2020;16(9):1903736. doi: 10.1002/smll.201903736

27. Jin Z, Zhai Y, Zhou Y, *et al*. Regulation of mesenchymal stem cell osteogenic potential via microfluidic manipulation of microcarrier surface curvature. *Chem Eng J.* 2022;448:137739. doi: 10.1016/j.cej.2022.137739

28. He Q, Zhang J, Liao Y, *et al*. Current advances in microsphere based cell culture and tissue engineering. *Biotechnol Adv.* 2020;39:107459. doi: 10.1016/j.biotechadv.2019.107459

29. Hendow EK, Iacoviello F, Casajuana Ester M, Pellet-Many C, Day RM. Hierarchically structured biodegradable microspheres promote therapeutic angiogenesis. *Adv Healthc Mater.* 2024;13(31):e2401832. doi: 10.1002/adhm.202401832

30. Wang Y, Kankala RK, Zhang J, *et al*. Modeling endothelialized hepatic tumor microtissues for drug screening. *Adv Sci.* 2020;7(21):2002002. doi: 10.1002/advs.202002002

31. Zhang Y, Ma C, Xie J, Ågren H, Zhang H. Black phosphorus/polymers: status and challenges. *Adv Mater.* 2021;37(33):2100113. doi: 10.1002/adma.202100113

32. Bai L, Han Q, Han Z, *et al*. Stem cells expansion vector via bioadhesive porous microspheres for accelerating articular cartilage regeneration. *Adv Healthc Mater.* 2023;13(3):2302327. doi: 10.1002/adhm.202302327

33. Dhanabalan KM, Gupta VK, Agarwal R. Rapamycin–PLGA microparticles prevent senescence, sustain cartilage matrix production under stress and exhibit prolonged retention in mouse joints. *Biomater Sci.* 2020;8(15):4308-4321. doi: 10.1039/D0BM00596G

34. Wang Y, Yuan X, Yu K, *et al*. Fabrication of nanofibrous microcarriers mimicking extracellular matrix for functional microtissue formation and cartilage regeneration. *Biomaterials*. 2018;171:118-132. doi: 10.1016/j.biomaterials.2018.04.033

35. Hu Z, Lin H, Wang Z, *et al*. 3D printing hierarchical porous nanofibrous scaffold for bone regeneration. *Small*. 2024; 21(2):2405406. doi: 10.1002/smll.202405406

36. Dai W, Li S, Jia H, *et al*. Indirect 3D printing CDHA scaffolds with hierarchical porous structure to promote osteoinductivity and bone regeneration. *J Mater Sci Technol*. 2025;207:295-307. doi: 10.1016/j.jmst.2024.04.032

37. He J, Sun Y, Gao Q, *et al*. Gelatin methacryloyl hydrogel, from standardization, performance, to biomedical application. *Adv Healthc Mater.* 2023;12(23):2300395. doi: 10.1002/adhm.202300395

38. Huang Z, Kraus VB. Does lipopolysaccharide-mediated inflammation have a role in OA? *Nat Rev Rheumatol.* 2016;12(2):123-129. doi: 10.1038/nrrheum.2015.158

39. Xue C, Tian J, Cui Z, *et al*. Reactive oxygen species (ROS)-mediated M1 macrophage-dependent nanomedicine remodels inflammatory microenvironment for osteoarthritis recession. *Bioact Mater.* 2024;33:545-561. doi: 10.1016/j.bioactmat.2023.10.032

40. Yu X, Gholipourmalekabadi M, Wang X, Yuan C, Lin K. Three-dimensional bioprinting biphasic multicellular living scaffold facilitates osteochondral defect regeneration. *Interdiscip Mater.* 2024;3(5):738-756. doi: 10.1002/idm2.12181

41. Jhun J, Min H-K, Na HS, *et al*. Combinatmarion treatment with *Lactobacillus acidophilus* LA-1, vitamin B, and curcumin ameliorates the progression of osteoarthritis by inhibiting the pro-inflammatory mediators. *Immunol Lett.* 2020;228:112-121.

doi: 10.1016/j.imlet.2020.10.008

42. Luo W, Bai L, Zhang J, *et al*. Polysaccharides-based nanocarriers enhance the anti-inflammatory effect of curcumin. *Carbohydr Polym*. 2023;311:120718. doi: 10.1016/j.carbpol.2023.120718

43. Liu X, Chen B, Chen J, *et al*. A cardiac-targeted nanozyme interrupts the inflammation-free radical cycle in myocardial infarction. *Adv Mater*. 2023;36(2):2308477. doi: 10.1002/adma.202308477

44. Yao Q, Yang Y, Hu M, Qiu Y, Shi Y, Kou L. Liposomal dexamethasone for intra-articular therapy: Functional strategies and clinical progress. *J Control Release*. 2025;385:114040. doi: 10.1016/j.jconrel.2025.114040

45. da Costa BR, Pereira TV, Saadat P, *et al*. Effectiveness and safety of non-steroidal anti-inflammatory drugs and opioid treatment for knee and hip osteoarthritis: network meta-analysis. *BMJ*. 2021;375:n2321. doi: 10.1136/bmj.n2321

46. Chen Y, Chen L-F, Wang Y, *et al*. Engineered dECM-based microsystem promotes cartilage regeneration in osteoarthritis by synergistically enhancing chondrogenesis of BMSCs and anti-inflammatory effect. *Compos B*. 2025;290:111974. doi: 10.1016/j.compositesb.2024.111974

47. Wu D, Yu Y, Zhao C, *et al*. NK cell-encapsulated porous microspheres via microfluidic electrospray for tumor immunotherapy. *ACS Appl Mater Interfaces*. 2019;11(37):33716-33724. doi: 10.1021/acsami.9b12816

48. Chen X, Zhang D, Wang X, *et al*. Preparation of porous GelMA microcarriers by microfluidic technology for stem-cell culture. *Chem Eng J*. 2023;477:146444. doi: 10.1016/j.cej.2023.146444

49. Long J, Yao Z, Zhang W, *et al*. Regulation of osteoimmune microenvironment and osteogenesis by 3D-printed PLAG/black phosphorus scaffolds for bone regeneration. *Adv Sci*. 2023;10(28):2302539. doi: 10.1002/advs.202302539

50. Wei J, Xia X, Xiao S, *et al*. Sequential dual-biofactor release from the scaffold of mesoporous HA microspheres and PLGA matrix for boosting endogenous bone regeneration. *Adv Healthc Mater*. 2023;12(20):2300624. doi: 10.1002/adhm.202300624

51. Dong R, Kang M, Qu Y, Hou T, Zhao J, Cheng X. Incorporating hydrogel (with low polymeric content) into 3D-printed PLGA scaffolds for local and sustained release of BMP2 in repairing large segmental bone defects. *Adv Healthc Mater*. 2024;14(2):2403613. doi: 10.1002/adhm.202403613

52. Kamboj N, Kazantseva J, Rahmani R, Rodríguez MA, Hussainova I. Selective laser sintered bio-inspired silicon-wollastonite scaffolds for bone tissue engineering. *Mater Sci Eng C*. 2020;116:111223. doi: 10.1016/j.msec.2020.111223

53. Zhu S, Bennett S, Kuek V, *et al*. Endothelial cells produce angiocrine factors to regulate bone and cartilage via versatile mechanisms. *Theranostics*. 2020;10(13):5957-5965. doi: 10.7150/thno.45422

54. Sun T, Feng Z, He W, *et al*. Novel 3D-printing bilayer GelMA-based hydrogel containing BP, β-TCP and exosomes for cartilage–bone integrated repair. *Biofabrication*. 2023;16(1):015008. doi: 10.1088/1758-5090/ad04fe

55. Liu S, Chen G, Chen Z, Wang F, Lv Y. Research progress on stiffness controllable scaffolds based on gelatin methacryloyl hydrogels for tissue repair and reconstruction. *Int J Biol Macromol*. 2025;321(Pt 3):146485. doi: 10.1016/j.ijbiomac.2025.146485

56. Matai I, Kaur G, Seyedsalehi A, McClinton A, Laurencin CT. Progress in 3D bioprinting technology for tissue/organ regenerative engineering. *Biomaterials*. 2020;226:119536. doi: 10.1016/j.biomaterials.2019.119536

57. Tong W, Chen X, Song X, *et al*. Resveratrol inhibits LPS-induced inflammation through suppressing the signaling cascades of TLR4-NF-κB/MAPKs/IRF3. *Exp Ther Med*. 2020;19(3):1824-1834. doi: 10.3892/etm.2019.8396

58. Lei J, Fu Y, Zhuang Y, Zhang K. Sema4D aggravated LPS-Induced injury via activation of the MAPK signaling pathway in ATDC5 chondrocytes. *Biomed Res Int*. 2020;2020:8691534. doi: 10.1155/2020/8691534

59. Peng K, Li Y, Lu C, Hu S. ABIN-1 protects chondrocytes from lipopolysaccharide-induced inflammatory injury through the inactivation of NF-κB signalling. *Clin Exp Pharmacol Physiol*. 2020;47(7):1212-1220. doi: 10.1111/1440-1681.13291

60. Yan F, Li H, Zhong Z, *et al*. Co-delivery of prednisolone and curcumin in human serum albumin nanoparticles for effective treatment of rheumatoid arthritis. *Int J Nanomedicine*. 2019;14:9113-9125. doi: 10.2147/ijn.S219413